

# *Ab initio* superionic-liquid phase diagram of $\text{Fe}_{1-x}\text{O}_x$ under Earth's inner core conditions

Zepeng Wu,<sup>1</sup> Chen Gao,<sup>1</sup> Feng Zhang,<sup>2</sup> Shunqing Wu,<sup>1</sup> Kai-Ming Ho,<sup>2</sup> Renata M. Wentzcovitch,<sup>3,4,5,6</sup> and Yang Sun<sup>1</sup>

<sup>1</sup>*Department of Physics, Xiamen University, Xiamen 361005, China*

<sup>2</sup>*Department of Physics, Iowa State University, Ames, IA 50011, USA*

<sup>3</sup>*Department of Applied Physics and Applied Mathematics,  
Columbia University, New York, NY 10027, USA*

<sup>4</sup>*Department of Earth and Environmental Sciences,  
Columbia University, New York, NY 10027, USA*

<sup>5</sup>*Lamont-Doherty Earth Observatory, Columbia University, Palisades, NY 10964, USA*

<sup>6</sup>*Data Science Institute, Columbia University, New York, NY 10027, USA*

(Dated: Oct. 30, 2024)

The superionic state represents a fundamental phase of matter where liquid-like mobility emerges within a solid crystalline lattice. This peculiar state has recently been discovered in the Earth's inner core. Despite extensive research on the kinetics of the superionic state and its geophysical impact on the Earth's core, the equilibration of the superionic phase with the liquid solution under core conditions has yet to be discovered. In this study, we develop a method to calculate the *ab initio* Gibbs free energy and the superionic-liquid phase diagram for the  $\text{Fe}_{1-x}\text{O}_x$  system under conditions near the Earth's inner core boundary. Our findings indicate oxygen can form superionic states in hcp and bcc iron. We elucidate the stability fields of these superionic phases, which vary significantly with oxygen stoichiometry. Furthermore, we show that the oxygen concentration in the Earth's inner core is likely higher than previously estimated due to the superionic state. This work offers a quantitative approach to studying the equilibrium between liquid and superionic solutions in Fe-light element systems under the extreme conditions of the Earth's core

## I. INTRODUCTION

Superionicity is a unique state where materials exhibit liquid-like mobility within a crystal lattice, drawing great interest in various scientific and industrial fields. Under ambient conditions, this property is crucial for solid electrolytes vital for next-generation all-solid-state batteries [1, 2]. At extremely high pressures and temperatures solid phases can also transform into superionic states [3–9], as is believed to occur with ice and ammonia solids in the mantles of Uranus and Neptune [10–16]. Recent simulations reveal that light elements like oxygen, hydrogen, and carbon can become superionic in hexagonal close-packed (hcp) iron under Earth's inner core (IC) conditions [17]. The kinetic behavior of the superionic state is proposed to cause the anisotropic seismic characteristics of the IC [18]. However, the stability field of the superionic state in the IC remains unclear. The phase competition between hcp and body-centered cubic (bcc) iron under IC conditions has long been debated [19, 20]. While recent studies suggest hcp as the stable phase [21, 22], it is uncertain if superionic states can emerge in bcc Fe-light element alloys and affect their stability relative to superionic hcp alloys under IC conditions. As light element compositions were determined based on hcp solution models [23, 24], superionic solutions could alter our understanding of light element partitioning between the solid IC and the liquid outer core. Thus, determining the thermodynamic stability of superionic phases, especially their equilibrium with liquid solutions at the inner core boundary (ICB), is crucial not only for fundamental physics in the novel state but also for constraining

the core's structure and chemical composition, which are vital for understanding the Earth's deep interior [19, 25].

Despite its importance, exploring the stability of the superionic phase in the inner core (IC) is challenging. Experimental proof of superionicity in Fe alloys is lacking due to the difficulty of detecting this state under IC conditions. Theoretical studies of phase competition among liquid, superionic, and solid phases are scarce, as calculating the free energy of the superionic state is highly non-trivial [26]. In the case of superionic ice, several attempts have been proposed to compute its free energy. A typical method is based on thermodynamic integration (TI), which provides the difference in free energy between the superionic phase and a reference model for which absolute free energy is known a priori. Although TI is accurate, finding a suitable reference for the superionic phase is difficult. Wilson et al. proposed using noninteracting harmonic oscillators and an ideal gas as a superionic reference [27]. However, this model suffers from the problem of particle overlap due to the lack of interactions between solid-like and liquid-like particles [28]. Cheng et al. used machine learning interatomic potentials to simulate the superionic and liquid coexistence for stoichiometric  $\text{H}_2\text{O}$  phases, providing melting curves for superionic  $\text{H}_2\text{O}$  [13]. While simulations of coexisting phases are sufficient to establish phase equilibria for stoichiometric systems such as  $\text{H}_2\text{O}$ , as we will demonstrate later, direct calculations of the absolute free energy for the liquid and superionic phases are necessary to obtain a complete phase diagram for the non-stoichiometric  $\text{Fe}_{1-x}\text{O}_x$  system. Besides, an extension from the empirical interatomic potential to the *ab initio* accuracy remains desirable. This interatomic

potential approach can serve as a reference model for computing the *ab initio* Gibbs free energy of the superionic state in TI. A similar method was recently developed to determine the melting temperatures and relative free energies of pure Fe phases under IC conditions [21], showing that classical simulations provide a suitable reference for *ab initio* calculations using TI or free-energy perturbation (FEP) methods [21, 29]. While this method is relatively straightforward for systems with constant stoichiometry like  $\text{H}_2\text{O}$  or Fe, it becomes more complex for non-stoichiometric solutions where the chemical potential of solute atoms in liquid and superionic phases is critical.

Here we develop a scheme to calculate the *ab initio* superionic-liquid phase diagram for the non-stoichiometric  $\text{Fe}_{1-x}\text{O}_x$  system under conditions close to Earth’s ICB. We construct a Fe-O interatomic potential to simulate the coexistence of superionic and liquid phases in  $\text{Fe}_{1-x}\text{O}_x$  systems using large-scale, long-timescale molecular dynamics (MD) simulations, which provide solidus and liquidus curves. Based on thermodynamic relations, we demonstrate it is possible to accurately compute the absolute Gibbs free energy for the superionic  $\text{Fe}_{1-x}\text{O}_x$  over a wide composition range. Using TI and FEP methods, we predict the *ab initio* Gibbs free energy of both liquid and superionic phases. This enables us to create a superionic-liquid phase diagram with *ab initio* accuracy. We elucidate phase competition between superionic hcp and bcc structures and assess the impact of the superionic state on oxygen partitioning between Earth’s inner and outer cores.

## II. METHODS

Classical MD simulations were performed using the Large-scale Atomic/Molecular Massively Parallel Simulator (LAMMPS) code [30]. The time step in the classical MD simulation was 1.0 fs. The Nosé-Hoover thermostat and barostat obeying modular invariance [31] were applied with a damping time  $\tau = 0.1$  ps. The nonequilibrium thermodynamic integration (TI) method [32] was employed to compute the Helmholtz free energy for the liquid solutions.

*Ab initio* molecular dynamics (AIMD) simulations were performed using the Vienna *ab initio* simulation package (VASP) [33, 34]. The projected augmented wave (PAW) method [35] was used to describe the electron-ion interaction. The generalized gradient approximation (GGA) in the Perdew-Burke-Ernzerhof (PBE) form [36] was employed for the exchange-correlation energy functional. The electronic entropy was included using the Mermin functional [37, 38], and the electronic temperature in the Mermin functional was the same as the ionic temperature. Supercells with 250, 288–293, and 250–254 atoms were used for liquid, superionic hcp, and superionic bcc phases, respectively. The time step in AIMD was 1 fs. The PAW potential with  $3d^74s^1$  valence elec-

trons (noted as PAW8) was used for Fe in the AIMD and TI. The PAW potential with  $3s^23p^63d^74s^1$  valence electrons (noted as PAW16) was used in the free energy perturbation (FEP). The PAW potential with  $2s^22p^4$  valence electrons was used for O. The plane-wave cutoff was 400 eV for PAW8-Fe and 750 eV for PAW16-Fe. The  $\Gamma$  point was used in the AIMD. A dense Monkhorst-Pack k-point mesh of  $2 \times 2 \times 2$  was adopted for superionic and liquid phases to achieve high DFT accuracy in the FEP calculations. For a target pressure, the lattice parameters of bcc, hcp, and liquid phases were adjusted for each temperature and composition to ensure that the pressure fluctuated around the target value by less than 0.5 GPa within 5 ps of simulations. The enthalpy data were collected from *ab initio* simulations lasting more than 10 ps.

## III. RESULTS

### A. Superionic-liquid coexistence

The key feature of the superionic  $\text{Fe}_{1-x}\text{O}_x$  alloy is the O diffusion in the crystalline lattice. Based on the *ab initio* MD simulation, we find O shows a similar mean squared displacement (MSD) in hcp, bcc, and liquid Fe phases at 323 GPa and 5500 K, a condition close to those at ICB (see Supplementary Information Fig. S3a). Thus, O is superionic in both hcp and bcc Fe under ICB conditions. Because *ab initio* MD simulation is highly limited by the time and length scales, we first use classical MD simulations to study the stability of superionic phases coexisting with liquid. Davies et al. [39] previously developed a Fe-O interatomic potential for IC conditions. While this potential can simulate the nucleation of Fe-O system [39], we find it failed to correctly describe the superionic state in  $\text{Fe}_{1-x}\text{O}_x$ . Here we developed a new Fe-O interatomic potential using the embedded-atom method [40](EAM) that accurately describes the superionic state in hcp and bcc lattices under ICB conditions (Supplementary Information Note 1). The MSD results from classical MD align qualitatively with *ab initio* simulations (Supplementary Information Fig. S3b).

To simulate the superionic hcp-liquid coexistence we constructed an hcp-liquid interface with 12,288 Fe atoms and randomly distributed O atoms for various O compositions. After a 2 ns MD simulation, O composition decreased in the hcp phase (Fig. 1a). The system reached equilibrium at around 100 ps, as indicated by the energy change in Fig. 1b. Extending the simulation to 2 ns showed that O atoms diffused throughout the simulation cell, providing sufficient data to compute their partitioning between hcp and liquid phases (Fig. 1c). The averaged O distribution suggests the O composition in the superionic phase ( $x_C^{SI}$ ) is significantly lower than that in the liquid phase ( $x_C^L$ ). Similar simulations across temperatures from 4600–6000 K at the same pressure yielded temperature-dependent  $x_C^{SI}$  and  $x_C^L$ , representing the su-

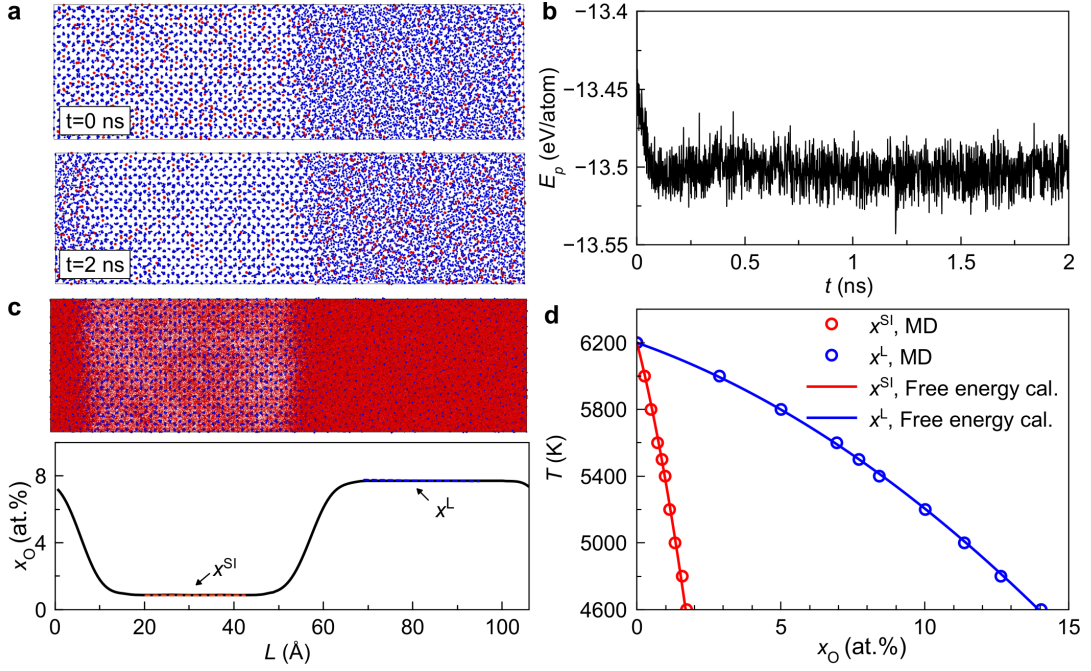


FIG. 1. Superionic-liquid coexistence simulations of  $\text{Fe}_{1-x}\text{O}_x$  solution. a, Initial and final configurations within 2 ns of superionic hcp-liquid coexistence at 323 GPa and 5500 K. The blue and red dots represent Fe and O atoms, respectively. b, Potential energy as a function of time in the simulation. c, O trajectory in last 1 ns. The lower panel shows the averaged O composition along the direction perpendicular to the interface. d, The phase diagram by classical MD simulation at 323 GPa. The circles are from direct superionic-liquid coexistence simulations. The lines are from free energy calculations.

perionic hcp solidus and liquidus lines (Fig. 1d).

### B. Free energy relations of superionic-liquid solutions

Based on the thermodynamic relations, when  $\text{Fe}_{1-x}\text{O}_x$  superionic solution coexists in equilibrium with the liquid solution at the temperature of  $T_0$ , it satisfies the equilibrium condition,

$$G_C^{SI}(x_{C_0}^{SI}, T_0) = G_C^L(x_{C_0}^L, T_0) - (x_{C_0}^L - x_{C_0}^{SI}) \left. \frac{\partial G_C^L(x, T_0)}{\partial x} \right|_{x=x_{C_0}^L} \quad (1)$$

where  $G_C^L(x_{C_0}^L, T_0)$  and  $G_C^{SI}(x_{C_0}^{SI}, T_0)$  are the absolute Gibbs free energies of the liquid and superionic phases with O compositions of  $x_{C_0}^L$  and  $x_{C_0}^{SI}$  at the temperature  $T_0$ , respectively (please refer to Supplementary Information Note 2 for detailed derivations). Since the MD simulation in Fig. 1 provides  $x_{C_0}^L$  and  $x_{C_0}^{SI}$  at various temperatures  $T_0$ , Eqn. (1) can be employed to compute the Gibbs free energy of the superionic phase  $G_C^{SI}(x_{C_0}^{SI}, T_0)$ , provided the liquid's Gibbs free energy  $G_C^L(x, T_0)$  is known (see Supplementary Information Note 3).

A series of free energy calculations for a liquid solution is performed across the O composition range of 0-20 at.% with the compositions spaced equally, at various temperatures, as shown in Fig. 2a. We find these liquid's free

energy data can be well described by the regular solution model using the Redlich-Kister (RK) expansion [41],

$$G(x, T_0) = G^{\text{Fe}}(T_0) + ax + x(1-x) \sum_{k=0}^n L_k (2x-1)^k + k_B T [x \ln x + (1-x) \ln(1-x)] \quad (2)$$

where  $G^{\text{Fe}}(T_0)$  is the Gibbs free energy of pure Fe,  $a$  and  $L_k$  are fitting parameters. Only two RK terms ( $k=0$  and 1) are required to fit the liquid's free energy data, achieving fitting errors of less than 0.1 meV/atom at all studied temperatures.

Based on Eqn. (1) and  $G_C^L(x, T_0)$ , we can compute  $G_C^{SI}(x_{C_0}^{SI}, T_0)$  for each  $(x_{C_0}^{SI}, x_{C_0}^L, T_0)$  combination obtained from MD simulations of superionic-liquid coexistence shown in Fig. 1. This results in sparse Gibbs free energy data for the superionic hcp state at a few temperatures, marked as solid circles in Fig. 2b. We then extend these data to a broader temperature range using the Gibbs-Helmholtz equation.

$$G(x_0, T) = \frac{T}{T_0} G(x_0, T_0) - T \int_{T_0}^T \frac{H(x_0, T)}{T^2} dT \quad (3)$$

Here,  $H(x_0, T)$  is the temperature-dependent enthalpy with a specific O composition  $x_0$  obtained from MD simulations. Using this approach,  $G_C^{SI}(x_{C_0}^{SI}, T)$  values are computed from  $G_C^{SI}(x_{C_0}^{SI}, T_0)$  and  $H(x_{C_0}^{SI}, T)$  for different

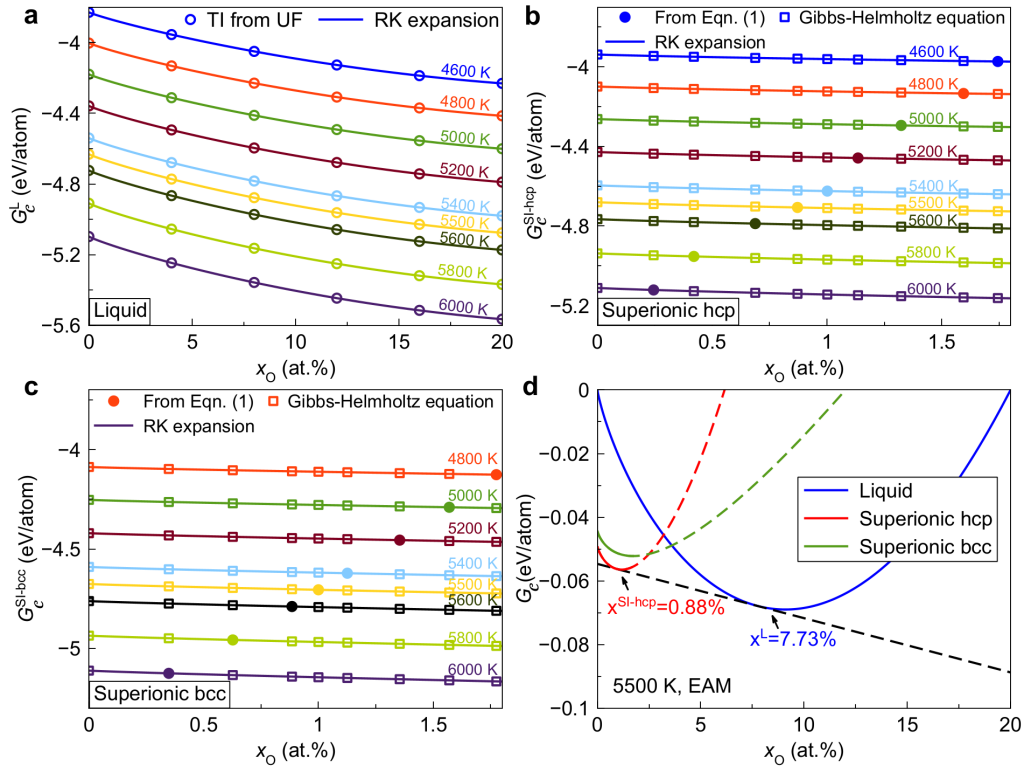


FIG. 2. Gibbs free energy calculations. a, The composition-dependent Gibbs free energy of liquid solutions with EAM potential at 323 GPa. The solid lines represent the fitting with the RK expansion. b, The composition-dependent Gibbs free energy of superionic hcp solutions. The solid circles are computed based on the superionic-liquid equilibrium condition in Eqn. (1). The open squares are computed based on the Gibbs-Helmholtz equation and the values of the solid circles. The solid lines represent the fitting with the RK expansion. c, The composition-dependent Gibbs free energy of superionic bcc solutions. d, The relative Gibbs free energy for liquid and superionic solutions at 323 GPa and 5500 K from EAM potential. The solid (dashed) line indicates the interpolated (extrapolated) results using RK expansion. The black dashed line is the common tangent line of Gibbs free energy for liquid and superionic hcp, which defines the solidus and liquidus composition.

$x_{C_0}^{SI}$ , and replotted as a function of compositions in Fig. 2b. We find that the free energy data of the superionic state can also be well-fitted by the RK expansion with only one RK term ( $k = 0$ ) to achieve a fitting error of less than 0.2 meV/atom.

With the absolute Gibbs free energy for both liquid and superionic solutions across various compositions and temperatures, the common tangent line approach can now provide the solidus and liquidus curves. We plot the relative Gibbs free energy using the 0% and 20% liquid free energy data as references for better visualization. Figure 2d shows the common tangent lines computed between  $G_C^{SI-hcp}(x)$  and  $G_C^L(x)$  curves at 5500 K, which resulted in intersections at  $x_{C_0}^{SI-hcp} = 0.88\%$  and  $x_{C_0}^L = 7.73\%$ . These values are consistent with the equilibrium compositions of  $x_{C_0}^{SI-hcp} = 0.87\%$  and  $x_{C_0}^L = 7.70\%$  obtained from superionic hcp-liquid coexistence simulations under the same pressure and temperature conditions shown in Fig. 1c. More free energy data and their common tangent lines at other temperatures are shown in Supplementary Information Fig. S4. The superionic hcp solidus and liquidus curves computed from the free energy calculations are compared with those from MD simulations in Fig.

1d. Both methods result in a consistent superionic-liquid phase diagram, validating each other.

Because Eqns. (1-3) work for both superionic hcp and bcc phases, we repeated the calculations for the superionic bcc structure. The temperature-dependent free energies of superionic bcc are shown in Fig. 2c. The superionic bcc solidus and liquidus curves are shown in Supplementary Information Fig. S5. Figure 2d compares the relative free energy between superionic bcc and superionic hcp at 5500 K. More comparisons at different temperatures are shown in Fig. S4. These data suggest that the superionic bcc is metastable compared to the superionic hcp phase when the O composition is small. When the O composition is greater than  $\sim 3$  at.%, the superionic bcc becomes more stable than superionic hcp in  $\text{Fe}_{1-x}\text{O}_x$ . However, the common tangent lines suggest when equilibrated with the liquid solution, the composition in the superionic phase is less than  $\sim 1$  at.%. Thus, based on the classical potential, only superionic hcp can coexist with liquid at ICB.

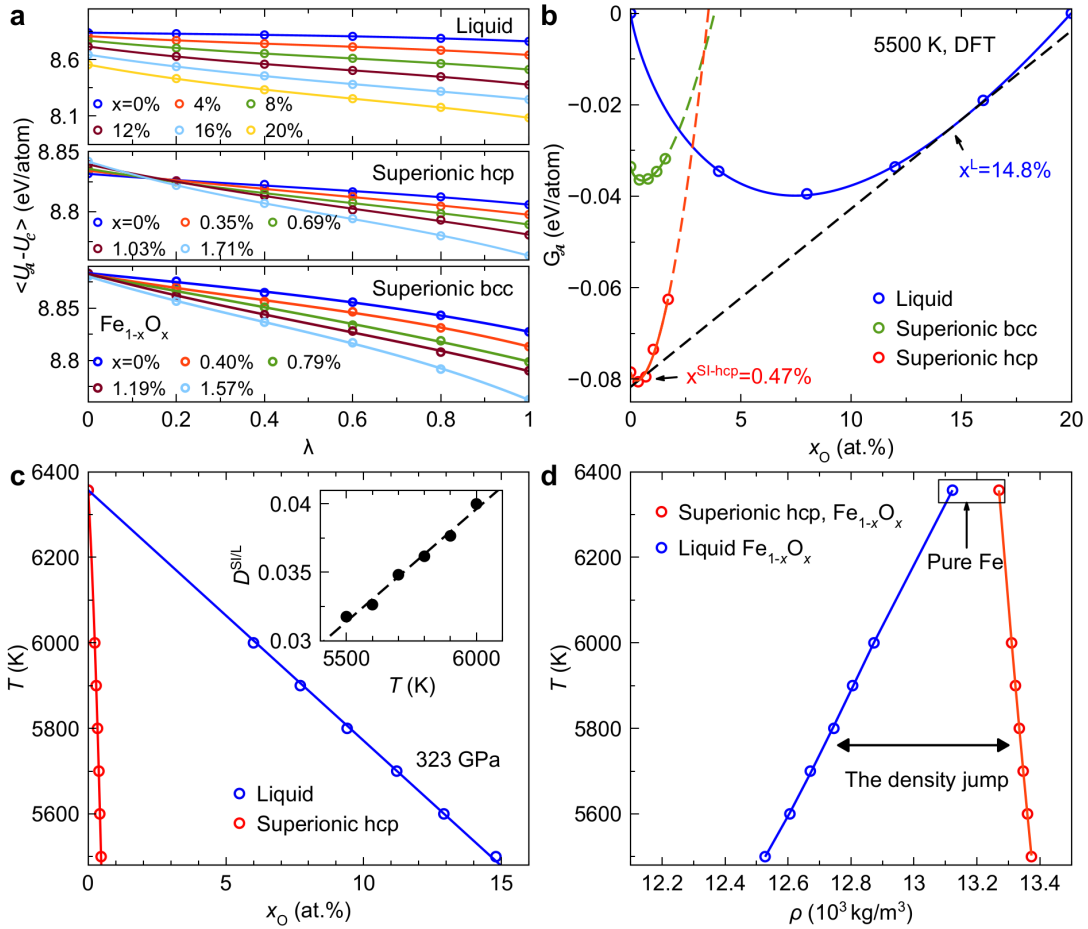


FIG. 3. *Ab initio* phase diagram of superionic and liquid  $\text{Fe}_{1-x}\text{O}_x$  solutions. a, The energy differences in the TI calculation from the classical to the ab initio system. The lines are the third-order polynomial fitting. b, The relative ab initio Gibbs free energy for liquid, superionic hcp, and superionic bcc solutions. The solid and dashed lines indicate the interpolated and extrapolated results using RK expansion, respectively. The black dashed line is the common tangent line. c, The superionic-liquid phase diagram of the  $\text{Fe}_{1-x}\text{O}_x$  superionic-liquid system at the ab initio level at 323 GPa. The inset shows the temperature dependent partition coefficient. d, Density of superionic hcp and liquid  $\text{Fe}_{1-x}\text{O}_x$  under the equilibrium composition at different temperatures.

### C. *Ab initio* Gibbs free energy of superionic phases

We have obtained the absolute Gibbs free energy,  $G_C$ , of the liquid and superionic solutions for the classical system. Using the classical system as the reference state, we can perform TI to compute the Gibbs free energy of liquid and superionic phases for the ab initio system (noted as A system). The formulas for such TI calculation are derived in Supplementary Information Note 4. A series of TI simulations from the classical system to the ab initio system were performed for liquid, superionic hcp, and superionic bcc solutions at 5500 K, as shown in Fig. 3a. The TI path from C to A system is smooth and almost linear for all three phases, suggesting great similarity between the classical and ab initio systems [21]. As the ab initio MD simulations were performed with PAW8 potential ( $3d^7 4s^1$  valence electrons), we further performed the FEP correction from PAW8 to PAW16 ( $3s^2 3p^6 3d^7 4s^1$  va-

lence electrons), as shown in Supplementary Information Fig. S8, which was demonstrated to be necessary for an accurate correction of the free energy data of Fe under Earth's core conditions [21, 42]

Figure 3b shows the relative *ab initio* Gibbs free energy for liquid and superionic phases at 5500 K and 323 GPa. The regular solution model with the RK expansion of Eqn. (2) can also describe the compositional dependence of these free energies, providing fitting errors of less than 0.5 meV/atom. This error is larger than those in classical systems, mainly due to fewer data points and smaller length scales in *ab initio* calculations. Nevertheless, such a free energy error is sufficiently small for phase diagram calculations. In Fig. 3b, the *ab initio* free energy of the superionic bcc phase is higher than the superionic hcp phase when the O composition is small. This is consistent with the fact that pure Fe prefers the hcp phase under IC conditions [21, 22]. As the O composition increases, the

free energy of the superionic hcp phase quickly increases. When the O composition is higher than  $\sim 3$  at.%, superionic bcc becomes more stable than superionic hcp. This trend is similar to the one found in the classical simulation. Thus, the O composition in  $\text{Fe}_{1-x}\text{O}_x$  changes the relative stability between the superionic bcc and hcp phases.

However, the common tangent line between liquid and superionic phases suggests that the superionic solution can only coexist with the liquid solution at small O compositions. Based on the  $G_A^{\text{SI-hcp}}(x)$  and  $G_A^L(x)$  curves, the common tangent line reveals *ab initio* solidus and liquidus points at 5500 K of  $x_{A_0}^{\text{SI-hcp}} = 0.47\%$  and  $x_{A_0}^L = 14.8\%$ , respectively. Superionic hcp is more stable than superionic bcc at such a small O composition. We further employ the Gibbs-Helmholtz equation, i.e., Eqn. (3), to extend the free energy data to other temperatures for all three phases, as shown in Supplementary Information Fig. S9. The superionic hcp solidus and liquidus curves are computed using the common tangent approach. These data provide the *ab initio* phase diagram of superionic hcp and liquid  $\text{Fe}_{1-x}\text{O}_x$  at 323 GPa in Fig. 3c. The superionic solidus line shows small temperature dependence, while the liquidus line depends on temperature more strongly. This results in a partition coefficient ( $D^{\text{SI/L}} = \frac{x_A^{\text{SI}}}{x_A^L}$ ) that is strongly temperature-dependent.

The phase diagram in Fig. 3b indicates that the equilibrium O compositions in the solid IC and liquid outer core are highly correlated with the temperature at ICB. It provides a stronger constraint on the core's composition and temperature than the one from the partition coefficient data alone. Based on the phase diagram, the densities of  $\text{Fe}_{1-x}\text{O}_x$  superionic and liquid solutions can be computed under the equilibrium conditions at different temperatures, as shown in Fig. 3d. In previous work [43], O was used to account for the large density difference between the solid and liquid core, i.e., the "density jump". By assuming O is the only light element and combining the partition coefficient with the density jump data, the O compositions in the solid core and liquid core were proposed to be  $0.2 \pm 0.1$  at.% and  $8.0 \pm 2.5$  at.% [43], respectively. We use the current density of superionic hcp and liquid  $\text{Fe}_{1-x}\text{O}_x$  solutions to match the density jump in the Preliminary Reference Earth Model [44]. It simultaneously constrains the O compositions as  $0.35 \pm 0.05$  at.% in the solid core and  $9.7 \pm 1.6$  at.% in the liquid core, and a temperature of  $5790 \pm 90$  K at ICB. Therefore, compared to the previous substitutional solid solution, the superionic phase nearly doubles O's solubility in hcp Fe under Earth's IC conditions. While the superionic bcc phase is metastable at this small O composition, it cannot be entirely excluded as we have seen that the bcc phase can be stabilized in Fe-Ni alloys [45]. If Ni is included, the Gibbs free energy of the superionic bcc phase is likely to be lowered in Fig. 3b. Thus, other elements' effects must be included to fully resolve

the core's composition and structure.

#### IV. CONCLUSION

We have demonstrated that the phase diagram of superionic-liquid solutions under ICB conditions can be obtained from the coexistence simulation and *ab initio* free energy calculations. By applying this method to the  $\text{Fe}_{1-x}\text{O}_x$  system, we clarify the relative stability among superionic bcc, superionic hcp, and liquid phases and the O compositions between superionic and liquid solutions under ICB conditions. The superionic hcp phase is more stable than the superionic bcc phase when the O composition is less than  $\sim 3$  at.%. Due to O's low solubility, only the superionic hcp phase coexists with the liquid in the  $\text{Fe}_{1-x}\text{O}_x$  system. The superionic state increases the O composition in hcp Fe compared to previous substitutional solid solution models under IC conditions. The solid/superionic-liquid phase diagram can constrain the core's composition and temperature at the ICB. These findings suggest that the superionic state under IC conditions is critical to understanding Earth's core structure and composition, and our work opens a new pathway to studying the phase diagram of superionic-liquid solutions under planetary interior conditions.

#### ACKNOWLEDGMENTS

Work at Xiamen University was supported by the National Natural Science Foundation of China (Grants Nos. T2422016, 42374108 and 12374015). R.M.W. acknowledges support from National Science Foundation (Grants Nos. EAR-2000850 and EAR-1918126). K.M.H. acknowledges support from National Science Foundation (Grant No. EAR-1918134). S. Fang and T. Wu from the Information and Network Center of Xiamen University are acknowledged for their help with GPU computing. The supercomputing time was partly supported by the Opening Project of the Joint Laboratory for Planetary Science and Supercomputing, Research Center for Planetary Science, and the National Supercomputing Center in Chengdu (Grants No. CSYYGS-QT-2024-15).

- 
- [1] Hull, S. Superionics: crystal structures and conduction processes. *Rep. Prog. Phys.* 67, 1233 (2004).
- [2] Li, Y. et al. A lithium superionic conductor for millimeter-thick battery electrode. *Science* 381, 50–53 (2023).
- [3] Demontis, P., LeSar, R. and Klein, M. L. New high-pressure phases of ice. *Phys. Rev. Lett.* 60, 2284 (1988).
- [4] Millot, M. et al. Nanosecond X-ray diffraction of shock-compressed superionic water ice. *Nature* 569, 251–255 (2019).
- [5] Hernandez, J.-A. and Caracas, R. Superionic-superionic phase transitions in body-centered cubic H<sub>2</sub>O ice. *Phys. Rev. Lett.* 117, 135503 (2016).
- [6] Hou, M. et al. Superionic iron oxide–hydroxide in Earth’s deep mantle. *Nat. Geosci.* 14, 174–178 (2021).
- [7] Queyroux, J.-A. et al. Melting Curve and Isostructural Solid Transition in Superionic Ice. *Phys. Rev. Lett.* 125, 195501 (2020).
- [8] Weck, G. et al. Evidence and Stability Field of fcc Superionic Water Ice Using Static Compression. *Phys. Rev. Lett.* 128, 165701 (2022).
- [9] Luo, C., Sun, Y. and Wentzcovitch, R. M. Probing the state of hydrogen in  $\delta$ -AlOOH at mantle conditions with machine learning potential. *Phys. Rev. Res.* 6, 013292 (2024).
- [10] Cavazzoni, C. et al. Superionic and metallic states of water and ammonia at giant planet conditions. *Science* 283, 44–46 (1999).
- [11] Redmer, R., Mattsson, T. R., Nettelmann, N. and French, M. The phase diagram of water and the magnetic fields of Uranus and Neptune. *Icarus* 211, 798–803 (2011).
- [12] Sun, J., Clark, B. K., Torquato, S. and Car, R. The phase diagram of high-pressure superionic ice. *Nat. Commun.* 6, 8156 (2015).
- [13] Cheng, B., Bethkenhagen, M., Pickard, C. J. and Hamel, S. Phase behaviours of superionic water at planetary conditions. *Nat. Phys.* 17, 1228–1232 (2021).
- [14] Gao, H. et al. Superionic silica-water and silica-hydrogen compounds in the deep interiors of Uranus and Neptune. *Phys. Rev. Lett.* 128, 035702 (2022).
- [15] Hernandez, J.-A. et al. Melting curve of superionic ammonia at planetary interior conditions. *Nat. Phys.* 19, 1280–1285 (2023).
- [16] Liu, C. et al. Multiple superionic states in helium–water compounds. *Nat. Phys.* 15, 1065–1070 (2019).
- [17] He, Y. et al. Superionic iron alloys and their seismic velocities in Earth’s inner core. *Nature* 602, 258–262 (2022).
- [18] Sun, S. et al. Superionic effect and anisotropic texture in Earth’s inner core driven by geomagnetic field. *Nat. Commun.* 14, 1656 (2023).
- [19] Hirose, K., Labrosse, S. and Hernlund, J. Composition and State of the Core. *Annu. Rev. Earth Planet. Sci.* 41, 657–691 (2013).
- [20] Belonoshko, A. B. et al. Stabilization of body-centred cubic iron under inner-core conditions. *Nat. Geosci.* 10, 312–316 (2017).
- [21] Sun, Y. et al. Ab initio melting temperatures of bcc and hcp iron under the earth’s inner core condition. *Geophys. Res. Lett.* 50, e2022GL102447 (2023).
- [22] González-Cataldo, F. and Militzer, B. Ab initio determination of iron melting at terapascal pressures and Super-Earths core crystallization. *Phys. Rev. Res.* 5, 033194 (2023).
- [23] Hirose, K., Wood, B. and Vočadlo, L. Light elements in the Earth’s core. *Nat. Rev. Earth Environ.* 2, 645–658 (2021).
- [24] Pozzo, M., Davies, C., Gubbins, D. and Alfè, D. FeO Content of Earth’s Liquid Core. *Phys. Rev. X* 9, 041018 (2019).
- [25] Poirier, J. P. Light elements in the Earth’s outer core: A critical review. *Phys. Earth Planet. Inter.* 85, 319–337 (1994).
- [26] Klarbring, J. and Simak, S. I. Phase stability of dynamically disordered solids from first principles. *Phys. Rev. Lett.* 121, 225702 (2018).
- [27] Wilson, H. F., Wong, M. L. and Militzer, B. Superionic to superionic phase change in water: consequences for the interiors of uranus and neptune. *Phys Rev Lett* 110, 151102 (2013).
- [28] Fidalgo Cândido, V., Matusalem, F. and de Koning, M. Melting conditions and entropies of superionic water ice: Free-energy calculations based on hybrid solid/liquid reference systems. *J. Chem. Phys.* 158, 064502 (2023).
- [29] Reinhardt, A. and Cheng, B. Quantum-mechanical exploration of the phase diagram of water. *Nat. Commun.* 12, 588 (2021).
- [30] Thompson, A. P. et al. LAMMPS—a flexible simulation tool for particle-based materials modeling at the atomic, meso, and continuum scales. *Comput. Phys. Commun.* 271, 108171 (2022).
- [31] Wentzcovitch, R. M. Invariant molecular-dynamics approach to structural phase transitions. *Phys. Rev. B* 44, 2358 (1991).
- [32] Paula Leite, R. and de Koning, M. Nonequilibrium free-energy calculations of fluids using LAMMPS. *Comput. Mater. Sci.* 159, 316–326 (2019).
- [33] Hafner, J. Ab-initio simulations of materials using VASP: Density-functional theory and beyond. *J. Comput. Chem.* 29, 2044–2078 (2008).
- [34] Kresse, G. and Furthmüller, J. Efficient iterative schemes for ab initio total-energy calculations using a plane-wave basis set. *Phys. Rev. B* 54, 11169 (1996).
- [35] Blöchl, P. E. Projector augmented-wave method. *Phys. Rev. B* 50, 17953 (1994).
- [36] Perdew, J. P., Burke, K. and Ernzerhof, M. Generalized gradient approximation made simple. *Phys. Rev. Lett.* 77, 3865 (1996).
- [37] Mermin, N. D. Thermal properties of the inhomogeneous electron gas. *Phys. Rev.* 137, A1441 (1965).
- [38] Wentzcovitch, R. M., Martins, J. L. and Allen, P. B. Energy versus free-energy conservation in first-principles molecular dynamics. *Phys. Rev. B* 45, 11372 (1992).
- [39] Davies, C. J., Pozzo, M. and Alfè, D. Assessing the inner core nucleation paradox with atomic-scale simulations. *Earth Planet. Sci. Lett.* 507, 1–9 (2019).
- [40] Daw, M. S. and Baskes, M. I. Embedded-atom method: Derivation and application to impurities, surfaces, and other defects in metals. *Phys. Rev. B* 29, 6443 (1984).
- [41] Redlich, O. and Kister, A. Algebraic representation of thermodynamic properties and the classification of solu-

- tions. *Ind. Eng. Chem.* 40, 345–348 (1948).
- [42] Sun, T., Brodholt, J. P., Li, Y. and Vočadlo, L. Melting properties from ab initio free energy calculations: Iron at the Earth’s inner-core boundary. *Phys. Rev. B* 98, 224301 (2018).
- [43] Alfe, D., Gillan, M. J. and Price, G. D. Composition and temperature of the Earth’s core constrained by combining ab initio calculations and seismic data. *Earth Planet. Sci. Lett.* 195, 91–98 (2002).
- [44] Dziewonski, A. M. and Anderson, D. L. Preliminary reference Earth model. *Phys. Earth Planet. Inter.* 25, 297–356 (1981).
- [45] Sun, Y. et al. Unveiling the effect of Ni on the formation and structure of Earth’s inner core. *Proc Natl Acad Sci U A* 121, e2316477121 (2024).